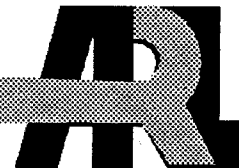*ARMY RESEARCH LABORATORY*

Mode I Large Strain Viscoelastic Crack Behavior in Nitrile Rubber Sheets

Claudia Quigley and Joey Mead

ARL-TR-513   October 1994

DTIC
ELECTE
S   JAN 2 6 1995
G   D

19950124 007

REPORT DOCUMENTATION PAGE

1. AGENCY USE ONLY (Leave blank)	2. REPORT DATE October 1994	3. REPORT TYPE AND DATES COVERED Final Report

4. TITLE AND SUBTITLE

Mode I Large Strain Viscoelastic Crack Behavior in Nitrile Rubber Sheets

5. FUNDING NUMBERS

6. AUTHOR(S)

Claudia J. Quigley and Joey L. Mead

7. PERFORMING ORGANIZATION NAME(S) AND ADDRESS(ES)

U.S. Army Research Laboratory
Watertown, MA 02172-0001
ATTN: AMSRL-MA-PC

8. PERFORMING ORGANIZATION REPORT NUMBER

ARL-TR-513

9. SPONSORING/MONITORING AGENCY NAME(S) AND ADDRESS(ES)

10. SPONSORING/MONITORING AGENCY REPORT NUMBER

11. SUPPLEMENTARY NOTES

12a. DISTRIBUTION/AVAILABILITY STATEMENT

Approved for public release; distribution unlimited.

12b. DISTRIBUTION CODE

13. ABSTRACT (Maximum 200 words)

A finite element analysis of a Mode I crack in a viscoelastic, hyperelastic, and incompressible material was performed under relaxation conditions. Loading of the finite element model was applied until the far field strain reached 50%; the viscoelastic material was then allowed to relax for 15 minutes. The numerical results were compared to experimental material behavior. The applied load and stretch ratio histories obtained from the finite element analysis agreed closely with experimental results. The S_{22} stress component was the dominant stress and possessed a singularity of $o(r^{-1})$, similar to the asymptotic solution for a mechanical crack tip stress field, which does not include viscoelasticity, in a hyperelastic material. The order of the singularity did not change with relaxation. Examination of the crack tip stress field showed that maximum stresses were found close to the crack surface suggesting that crack propagation should initiate above and below the deformed crack tip.

14. SUBJECT TERMS

Mode I fracture, Large strain viscoelasticity, Nitrile rubber, Finite element analysis

15. NUMBER OF PAGES

36

16. PRICE CODE

17. SECURITY CLASSIFICATION OF REPORT	18. SECURITY CLASSIFICATION OF THIS PAGE	19. SECURITY CLASSIFICATION OF ABSTRACT	20. LIMITATION OF ABSTRACT
Unclassified	Unclassified	Unclassified	UL

Contents

Figures

iii

Tables

Introduction

Elastomer and rubber components are found on many U.S. Army vehicles, including tires, bushings, and track pads. An improved understanding of the failure process in elastomers would assist materials scientists in the design of new and stronger rubberlike materials and would aid structural engineers in the design of rubber components with improved service life. The ability to model simple fracture behavior under large strains in a viscoelastic, hyperelastic, and incompressible material is an important step towards modeling crack growth in elastomers.

When viscoelastic materials undergo a constant strain, the applied stress diminishes with time. Although viscoelasticity is known to affect crack tip behavior in hyperelastic and incompressible materials, its contribution has not been quantified. In this investigation, a model for nonlinear viscoelastic material behavior in a Mode I crack was examined. A finite element analysis of a Mode I Single Edge Notched (SEN) elastomer specimen under relaxation conditions was performed and compared to experimental data. Changes in the stress field with time were examined. The tearing energy was also studied as a function of time.

Tearing Energy

The tearing energy, T, was first defined by Rivlin and Thomas [1] as the energy released per unit area as a crack of length L advances by $\delta\ell$. Mathematically, the tearing energy is represented as

$$T = \frac{1}{b}\left[\frac{\partial U}{\partial L}\right]_{\delta\ell} , \tag{1}$$

where U is the total strain energy stored through elastic deformation and b is the specimen

1

thickness. When the release of stored strain energy is greater than the energy required to generate new surface area, the crack will propagate. The tearing energy is equivalent to the J-integral[2] for nonlinear elastic materials. For a crack advancing in the x_1 direction, refer to Figure 1,

$$J = \int_{\Gamma} [W n_1 - t_i u_{i,1}] dS \qquad (2)$$

where W represents the strain energy density, n_1 is the component of the unit normal in the x_1-direction, t_i is the nominal traction vector, and u_i is the displacement vector. The J-integral is path independent when evaluated along any suitable contour Γ in the reference configuration which encompasses the crack tip, while dS is an element of arc length along Γ. For hyperelastic materials, the J-integral is globally path independent and equals the energy release rate. For viscoelastic materials, care must be taken in the interpretation of the J-integral. The global path independence of J applies only when the stress is a single valued function of strain. For a Mode I crack under relaxation conditions, this condition is met. When the applied stresses are infinitesimal, the J-integral is a function of the stress intensity factor, K_I, or

$$J = \frac{K_I^2}{3\mu} \qquad (3)$$

under plane stress conditions, where μ is the infinitesimal shear modulus.

Experimental Procedures

The material used in this study was a carbon black filled, highly saturated nitrile rubber (HNBR) cured with peroxide and a zinc dimethacrylate co-curative. It is based on a formulation

2

Table 1: MATERIAL FORMULATION

Ingredient	phr
HNBR (Zeptol 2020[a])	100.0
N-121 Carbon Black	20.0
Zinc Oxide	2.0
Agerite Resin D[b]	0.5
Zinc Dimethacrylate coagent[c]	30.0
Dicumyl Peroxide (Dicup R)[d]	1.3

[a] Zeon Chemicals, ACN 36%, unsaturation 10%

[b] R. T. Vanderbilt, Polymerized 1,2 - dihydro - 2,2,4 - trimethylquinoline

[c] Sartomer, SR - 634

[d] Hercules

developed for use in tank track pads [3] and was supplied by Zeon Chemicals. Its formulation is given in Table 1.

Experimental tests were performed using an Instron model 4505 screw type machine with an Instron model elastomer extensometer attachment. The use of an extensometer to measure strain, rather than crosshead displacement, eliminates measurement error from slippage. Pneumatic/hydraulic grips were used with pressures from 7 to 10 MPa. Load and extension data were electronically captured. Strip specimens, measuring 15.24 by 2.54 cm, were die cut

from standard tensile sheets. The specimen was subjected to conditioning between 40% and 200% tensile strain at a strain rate of 2%/sec for 10 cycles. The conditioning was performed to reduce the Mullins effect. After the specimen was unloaded and removed from the grips, it was allowed to relax for 15 minutes. A crack of length 0.64 cm was then introduced along the mid-height of the specimen with a razor blade.

After conditioning and introducing the crack, the specimen was reinserted into the test machine. The specimens were pulled at a crosshead rate of 0.5%/sec to 50% strain and the load history was recorded for 15 minutes. In order to accurately capture the peak stress, the data was recorded at a speed of 10 points/sec for the first five minutes. Thereafter, the rate at which data was recorded was decreased to two points/sec. The specimen was then unloaded and removed from the grips.

Nonlinear Viscoelasticity

The mathematical basis [4, 5] for finite strain viscoelasticity will now be reviewed, focusing on the Prony series, which is used to model large strain viscoelastic material behavior. The implementation of the Prony series in ABAQUS [6], the commercial finite element software used in this analysis, will also be presented. Consider a spatial or deformed coordinate system, $\mathbf{y}(\mathcal{T})$, at time $\mathcal{T}$, and a material coordinate system, $\mathbf{x}$, in an isotropic, homogeneous and incompressible material. The deformation gradient is represented by $\mathbf{F}$, where

$$\mathbf{F}(\mathcal{T}) = \frac{\partial \mathbf{y}(\mathcal{T})}{\partial \mathbf{x}} \ . \tag{4}$$

4

A relative deformation gradient at time T relative to time t can be defined as

$$\mathbf{F}(T,t) = \frac{\partial \mathbf{y}(T)}{\partial \mathbf{y}(t)} \ , \tag{5}$$

where

$$\mathbf{F}(T,t) = \mathbf{F}(T)\mathbf{F}^{-1}(t) \ . \tag{6}$$

Under the assumptions of incompressibility, the determinant of F equals one. The left and right deformation tensors, B and C, are respectively

$$\mathbf{B} \ = \ \mathbf{F}\mathbf{F}^{\mathbf{T}} \ ,$$

and $\tag{7}$

$$\mathbf{C} \ = \ \mathbf{F}^{\mathbf{T}}\mathbf{F} \ ,$$

while the strain invariants, I_i, are

$$I_1 \ = \ tr\mathbf{C} \ ,$$

$$\tag{8}$$

$$I_2 \ = \ \frac{1}{2}\left(I_1^2 - tr\mathbf{C}^2\right) \ . $$

For incompressible materials, I_3 equals one. The Cauchy strains, E, are given in terms of the right deformation tensor, C, as

$$\mathbf{E} = \frac{1}{2}\left[\mathbf{C} - \mathbf{I}\right] \ , \tag{9}$$

Here, I is the identity matrix.

The deviatoric stress tensor, $\mathbf{S_e}$, is defined as

$$\mathbf{S_e} = 2\left[\frac{\partial W_e}{\partial I_1} + I_1\frac{\partial W_e}{\partial I_2}\mathbf{B} - \frac{\partial W_e}{\partial I_2}\mathbf{B}^2\right] \ , \tag{10}$$

where W_e is the elastic strain energy density. For hyperelastic materials, W_e can be expressed as a function of the strain invariants. Common examples include the Rivlin constitutive model and the Neo-Hookean material law.

The Cauchy stress, **S**, is represented by

$$\mathbf{S} = \mathbf{S_e} - p\mathbf{I} \ . \tag{11}$$

The indeterminate pressure, p, is a consequence of incompressibility and is found through the applied boundary conditions and equilibrium. The nominal stress, σ, can be defined in terms of the Cauchy stress as

$$\sigma = SF^{-T} \ . \tag{12}$$

The viscoelastic Cauchy stresses are now expressed as

$$\mathbf{S} = \mathbf{S_e} - p\mathbf{I} + \int_{-\infty}^{t} \mathbf{F}^{-1}(\mathcal{T},t)\frac{\partial W_v}{\partial \mathbf{E}}\mathbf{F}^{-T}(\mathcal{T},t)d\mathcal{T} \ , \tag{13}$$

In this equation, the viscoelastic strain energy density, W_v, is a measure of the energy dissipated by the material and must be measured from creep or relaxation experiments. Consequently, the function $\partial W_v/\partial \mathbf{E}$ will decay or fade in time and can be described by a monotonically decreasing function. Although many potential forms of $\partial W_v/\partial \mathbf{E}$ are possible, a common assumption is that W_v is the product of separable functions of time and strain throughout the relaxation spectrum. A Prony series can be used to model the viscoelastic response, as demonstrated by Quigley [7], Johnson [8], and Schapery [9] so that

$$\frac{\partial W_v}{\partial \mathbf{E}} = \sum_{m=1}^{M} P_m exp(t - \mathcal{T})/\tau_m \ , \tag{14}$$

where each time constant, τ_m, is paired with a multiplicative scalar, P_m.

6

Constitutive Model

The finite element analysis was performed with ABAQUS [6] which assumes that W_v has the same form as W_e. The multiplicative constants, P_m, are provided as nondimensional fractions, g_m, of a hyperelastic energy function, W, so that

$$P_m = \frac{\partial W}{\partial \mathbf{E}} g_m \ , \tag{15}$$

where

$$\frac{\partial W_e}{\partial \mathbf{E}} = g_{longterm} \frac{\partial W}{\partial \mathbf{E}} \ , \tag{16}$$

and

$$\frac{\partial W_v}{\partial \mathbf{E}} = \sum_{k=1}^{K} g_k exp[t - \mathcal{T}/\tau_k] \frac{\partial W}{\partial \mathbf{E}} \ . \tag{17}$$

It is also assumed that

$$g_{longterm} + \sum_{k=1}^{K} g_k = 1 \ . \tag{18}$$

Therefore, W specifies the overall shape and magnitude of the combined elastic (long term) and viscoelastic material behavior. The proportion of the material behavior that is viscoelastic is governed by $\sum_{k=1}^{K} g_k$, while the proportion of long term material behavior is determined by $g_{longterm}$. Here, W was arbitrarily selected as the Rivlin constitutive law, or

$$W = \sum_{i=0}^{n} \sum_{j=0}^{n} C_{ij}(I_1 - 3)^i (I_2 - 3)^j; C_{00} = 0 \ , \tag{19}$$

where I_1 and I_2 are functions of the stretch ratios, λ_i,

$$I_1 \quad = \quad \lambda_1^2 + \lambda_2^2 + \lambda_3^2 \ ,$$

$$\tag{20}$$

$$I_2 \quad = \quad \lambda_1^2 \lambda_2^2 + \lambda_2^2 \lambda_3^2 + \lambda_1^2 \lambda_3^2 \ ,$$

and where C_{ij} are time independent material constants. In uniaxial extension, the stretch ratios can be expressed as

$$\lambda_1 = \lambda \ ,$$

(21)

$$\lambda_{2,3} = 1/\lambda^{1/2} \ .$$

At an arbitrary time, t, the expression for nominal uniaxial stress in a step - strain relaxation test, based on Equations (10), (12), (13), (16), and (17), becomes

$$\sigma(\lambda,t) = 2(\lambda - 1/\lambda^2)\left[\frac{\partial W}{\partial I_1} + 1/\lambda\frac{\partial W}{\partial I_2}\right]\left(g_{longterm} + \sum_{k=1}^{K} g_k exp[-t/\tau_k]\right) \ .$$

(22)

As $t \rightarrow 0$, substituting Equation (18) into the above expression for uniaxial stress yields

$$\sigma(\lambda,0) = \left(\lambda - \frac{1}{\lambda^2}\right)\left(\frac{\partial W}{\partial I_1} + \frac{1}{\lambda}\frac{\partial W}{\partial I_2}\right) \ ,$$

(23)

and stress strain behavior can be approximated from a "quick pull" test. Because $\sigma(\lambda,0)$ is only a function of W, the material constants, C_{ij}, can now be found. Previous studies [7] determined the material constants for this HNBR elastomer so that the resulting constitutive model would be stable in a Drucker sense. These time independent material constants were given the following values:

$$C_{01} = 1.05 MPa \text{ and } C_{30} = 0.76 \times 10^{-3} MPa.$$

(24)

A Prony series was determined from relaxation data[7] for this material. The values of the multiplicative constants were again constrained to assure Drucker stability and are listed in Table 2. A comparison of predicted material behavior and experimental data is shown in Figure 2 for a 0.5%/sec single cycle hysteresis loop to 200% strain.

Table 2: TIME DEPENDENT MATERIAL CONSTANTS IN PRONY SERIES

τ_k	$g_k \times 10^{-2}$
0.1778	5.18
0.3162	4.04
1.0000	7.19
1.7783	2.47
3.1623	4.91
5.6234	3.35
10.000	7.23
31.623	7.00
56.234	2.88
177.83	1.61
316.23	8.46

Mechanical Crack Tip Stress Field

There is no theoretical asymptotic solution for a Mode I crack in a viscoelastic, hyperelastic and incompressible material. Therefore, for this analysis the far field loads and displacements from the finite element analysis will be compared to the experimental results. Because experimental data close to the crack tip could not be measured, numerically determined crack tip field quantities cannot be verified.

Asymptotic crack tip fields have been derived for the mechanical crack tip Mode I stress field in hyperelastic and incompressible materials. For completeness, both the linear elastic crack tip field and the Mode I crack tip field in a Neo-Hookean material will be presented. At the crack tip, a polar coordinate system was introduced such that

$$x_1 = r \cos \theta, \qquad x_2 = r \sin \theta. \tag{25}$$

The linear elastic asymptotic solution [10] is

$$
\begin{aligned}
\sigma_{11} &= \frac{K_I}{\sqrt{2\pi r}} \cos \frac{\theta}{2} \left(1 - \sin \frac{\theta}{2} \sin \frac{3\theta}{2}\right) + o\left(r^{1/2}\right) , \\
\sigma_{22} &= \frac{K_I}{\sqrt{2\pi r}} \cos \frac{\theta}{2} \left(1 + \sin \frac{\theta}{2} \sin \frac{3\theta}{2}\right) + o\left(r^{1/2}\right) , \\
\sigma_{12} &= \frac{K_I}{\sqrt{2\pi r}} \cos \frac{\theta}{2} \cos \frac{3\theta}{2} \sin \frac{\theta}{2} + o\left(r^{1/2}\right) ,
\end{aligned}
\tag{26}
$$

where σ_{ij} represents the nominal stresses, and K_I is the stress intensity factor. This solution would be present in the crack tip region only if the far field strains were infinitesimal and viscoelastic stresses were absent.

A Neo-Hookean material is based on the linear, one term form of the Rivlin law, Equation(19),

$$W = C_{10}(I_1 - 3) . \tag{27}$$

10

The plane stress nonlinear asymptotic crack tip field for this material was derived by Knowles and Sternberg [11] as

$$S_{11} \sim o(r^{-1/2}) \;,$$

$$S_{22} \sim \frac{\mu}{4} a^2 r^{-1} \;,$$

$$S_{12} \sim -\frac{\mu}{2} ab r^{-1/2} \sin\frac{\theta}{2} \;, \qquad (28)$$

$$y_1 \sim \frac{r}{b} \cos\theta \;,$$

$$y_2 \sim a r^{1/2} \sin\frac{\theta}{2} \;,$$

where the Cauchy stresses, S_{ij}, and the deformation field, y_i, are referenced to the polar coordinate system (r, θ) in the undeformed configuration. The load amplitude constants, a and b, are functions of the applied load and the geometry.

Finite Element Model

A finite element model of the SEN test specimen is provided in Figure 3. Only the top half of the specimen was modeled due to reflective symmetry about the x_1 axis. The crack tip region is modeled by a semicircular mesh containing both refined and coarse regions. This mesh design in the crack tip region can sustain large deformations at the crack tip so that nonlinear stresses can be more accurately determined. At these large deformations, numerical mapping methods typically break down, and the elements begin to evert, making the nonlinear crack tip field difficult to resolve. Consequently, the finite element mesh was composed of two regions, a coarse mesh in the immediate vicinity of the crack tip, enclosed by a refined mesh,

11

where accurate crack tip field quantities could be found. The coarse mesh circumvented the numerical problems described above and allowed the nonlinear crack tip field to extend into the refined mesh region. In addition, the coarse mesh region was sufficiently small so that it did not significantly influence crack tip field quantities in the adjacent refined mesh region. Both the coarse mesh and the refined mesh contained rings of eight-noded isoparametric elements. Within a ring, all elements had equal angular extent and the same radial length.

The circumferentially coarse mesh, as shown in Figure 4(a), had three rings of elements and extended radially to 2.54×10^{-3} cm. The first ring was constructed of three elements of radius 2.54×10^{-4} cm. In each subsequent ring, the number of elements was doubled so that the fourth ring contained 24 elements. Along each circumferential element ring, nodal displacements were constrained to enforce compatibility.

The surrounding refined mesh, partially shown in Figure 4(b), extended from 2.54×10^{-3} to 0.254 cm. Each of the circumferential twenty-four rings in the refined mesh were constructed of 24 elements. Element radii were biased such that, along a radius extending from the crack tip, they were equally spaced on a logarithmic scale from 2.54×10^{-3} to 2.54×10^{-1} cm. Within each decade cm unit of crack length, $10^{-(m+1)}$ to 10^{-m}, where m ranged from -3 to -1, were 12 rings of elements. There were 21 elements in the coarse mesh and 144 elements in the refined mesh, for a total of 165 elements surrounding the crack tip. Away from the crack tip region, the mesh was transitioned to a rectangular grid. The entire mesh contained 779 elements and 2577 nodes, with two kinematic degrees of freedom at each node and one additional pressure degree of freedom at each corner node.

12

Displacement boundary conditions were applied along the top of the specimen, as shown in Figure 5, as a function of time. The displacements uniformly increased with time for 88 sec. At this time, the stretch ratios close to the top of the specimen equalled 1.5, while stresses should be at maximum values throughout the test specimen. From 88 to 900 sec, the displacements were fixed, allowing stress relaxation to occur. The applied displacement history duplicated the one applied during the actual experiment.

Results

Comparison of finite element results to experimental data verified that the finite element analysis did simulate the experiment. Figures 6 and 7 show that the experimentally applied stretch ratios and stresses agreed closely with numerical data. The applied stretch ratios based on numerical results were centroidal values obtained from rows of elements across the top portion of the finite element mesh. The applied stretch ratios increased steadily with the experimentally applied strain rate to a maximum value of 1.5 at 88 sec, then remained constant for the rest of the experiment. Applied stresses were calculated from reaction forces across the top half the specimen. These stresses reached their peak value at 88 sec, when the applied stretch ratio of 1.5 was attained, and then steadily decreased, mimicking the experimentally observed viscoelastic behavior.

Energy changes in the mesh are found in Figure 8. The total energy in the specimen is the sum of the recoverable strain energy and the viscoelastic energy. The recoverable strain energy was maximum at 88 sec and then slowly decreased, similar to the applied stresses. The

viscoelastic energy quantity measured in ABAQUS [6] represented the energy loss in the finite element model due to viscous effects (time dependent behavior). The viscoelastic energy in the test specimen increased steadily until the maximum applied stretch ratio was reached. The viscoelastic energy continued to increase during the relaxation portion of the experiment, but at a slower rate.

The J-integral was determined by ABAQUS[6] over 16 paths, where each path was a circle encompassing the crack tip. Global path independence was maintained over the course of the entire analysis, as there was only a maximum difference of 3 % between the highest and lowest values of the J-integral at any given time. Average values of the J-integral as a function of time are provided in Figure 9. The J-integral increased until the maximum applied displacement was attained, and then decreased as viscoelastic energy losses occurred, making less energy available for crack growth.

The deformed finite element mesh at time t = 21 sec, as shown in Figure 10, showed the immediate development of a parabolic shape along the crack surface and blunting at the crack tip upon load application. The blunting became more pronounced with load application until t = 88 sec, as shown in Figure 11. After t = 88 sec, the deformed shape did not change while the specimen was relaxing.

Stresses in the refined crack mesh region were studied as plots of radial distance from the crack tip, where r refers to the undeformed element radius, and as plots of the undeformed polar angle, θ. Only centroidal values of stress were plotted. Radial plots of S_{22}, found in Figure 12, showed a change in slope with increased time and load application. At t = 21

14

sec ($\lambda = 1.1$), the slope of S_{22} was constant and equalled 1/2. At t = 88 sec ($\lambda = 1.5$), the slope of S_{22} changed with distance from the crack tip. Close to the crack tip, the slope was approximately one. However, with increasing distance from the crack tip, the slope decreased. These results suggest that

$$S_{22} \sim o(r^{-1/2}) \text{ for } \lambda_\infty \sim 1.1 \ .$$

$$(29)$$

$$S_{22} \sim o(r^{-1}) \text{ for } \lambda_\infty \sim 1.5 \ .$$

At $\lambda \sim 1.1$, strains far from the crack tip were close to linear behavior. It is noted that the linear S_{22} stress component is also of $o(r^{-1/2})$ (refer to Equation (26)). In addition, for S_{22} in the nonlinear plane stress asymptotic crack tip field for a Neo-Hookean material, see Equation (28), is also of $o(r^{-1})$. These dominant stresses appear to be consistent with crack tip fields in which viscoelasticity effects are not included. During relaxation, when $t > 88$ sec and $\lambda = 1.5$, the slope of S_{22} was unchanged while the stresses gradually decreased with time.

These results confirmed the significance of viscoelasticity as a fracture arrest mechanism which constrains crack growth. When a crack grows, the newly created surface area becomes traction free. As this new surface unloads, it undergoes viscoelastic softening, making less energy available for continued crack extension. These energy losses were demonstrated here by the increase in viscoelastic energy with relaxation, as shown in Figure 8. At the crack tip, documentation of the sustained energy losses as a function of time was found in both the J-integral, Figure 9, and the S_{22} stress component, Figure 12.

Examination of circumferential plots of stress as a function of the undeformed polar angle,

15

θ, revealed that maximum values of all three Cauchy stress components were found near the undeformed crack flank, behind the crack tip (refer to Figures 13 to 15). This behavior was found in a highly localized region surrounding the crack tip at small radii for $\lambda = 1.1$. The localized region continued to expand in size until the peak stretch ratio, $\lambda = 1.5$, was applied. The shape of the circumferential plots changed with radial distance from the crack tip, indicating a transition in the stress field. Close to the crack tip, the mechanical crack tip stress field was found. With increasing distance from the crack tip, the stress field changed to a transitional stress state governed by the presence of the crack tip, the specimen geometry, and the applied load. This stress state was shown at the larger radii in Figures 13 to 15.

Assuming that material failure occurs at sites of maximum stress, these plots indicate that failure is more likely to occur close to the crack surface, behind the crack tip and suggest that crack growth is likely to commence in this region. Experimental evidence [12, 13] of crack growth in plane stress SEN and other test specimens supports this hypothesis. These studies suggest that secondary crack growth occurs above and below the crack tip. A plane strain finite element analysis[14] also predicts that secondary crack growth should initiate close to the crack surface.

Future Work

For a better understanding of viscoelastic material behavior in the fracture process of elastomers, additional experimental and analytical research is required. Careful experimental studies of crack propagation on cracks of varying lengths are needed to measure the tearing energy

16

at the onset of crack propagation, as well as the direction and increment of crack growth. Finite element analysis of these specimens would allow us to monitor changes in stress fields and energy surrounding the crack tip before and after propagation.

References

[1] R. S. Rivlin and A. G. Thomas, *Journal of Polymer Sci.* **10** (1953) 291-318.

[2] J. R. Rice, *Journal of Applied Mechanics* **35** (1968) 379 - 386.

[3] P. Touchet, G. Rodriguez, P. E. Gatza, D. P. Butler, D. Crawford, A. R. Teets, H. O. Feuer, and D. P. Flanagan, U. S. Patent 4,843,114, June 27, 1989.

[4] J. D. Ferry, "Viscoelastic Properties of Polymers", John Wiley & Sons, New York, 1980.

[5] L. E. Malvern, "Introduction to the Mechanics of a Continuous Medium", Prentice - Hall, Inc., Englewood Cliffs, N.J., 1969.

[6] ABAQUS, Version 5.3, Hibbitt, Karlsson, and Sorensen, Inc., Providence, R.I.

[7] C. J. Quigley, J. L. Mead, and A. R. Johnson, submitted for publication to *Rubber Chemistry & Technology*

[8] A. R. Johnson, C. J. Quigley, and J. L. Mead, accepted for publication in *Rubber Chemistry & Technology*

[9] R. A. Schapery, Proc. *Fourth U.S. Nat. Cong. Appl. Mech.* **2**, (1962) 1075 - 1096.

[10] M. L. Williams, *Journal of Applied Mechanics* **24** (1957) 109 - 114.

[11] J. K. Knowles and E. Sternberg, *Journal of Elasticity* **13** (1983) 257 - 293.

[12] A. N. Gent and C. T. R. Pulford, *Journal of Material Science* **19** (1984) 3612 - 3619.

[13] C.J. Quigley, D.M. Parks, and R. Dooley, *Rubber Chemistry & Technology* **66** (1993) 156 - 173.

[14] C.J. Quigley and D.M. Parks, *International Journal of Fracture* **65** (1994) 75 - 96.
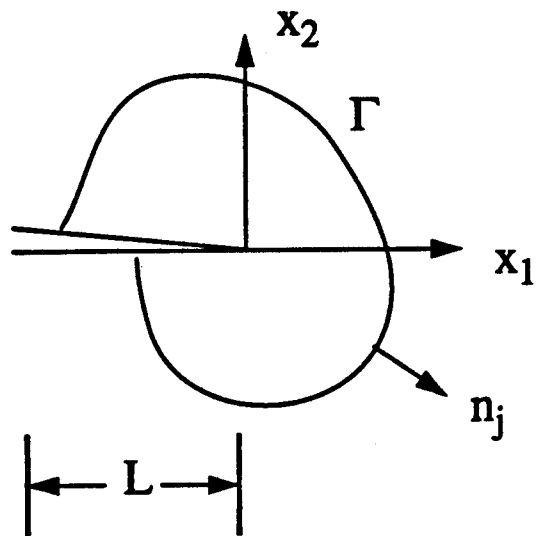
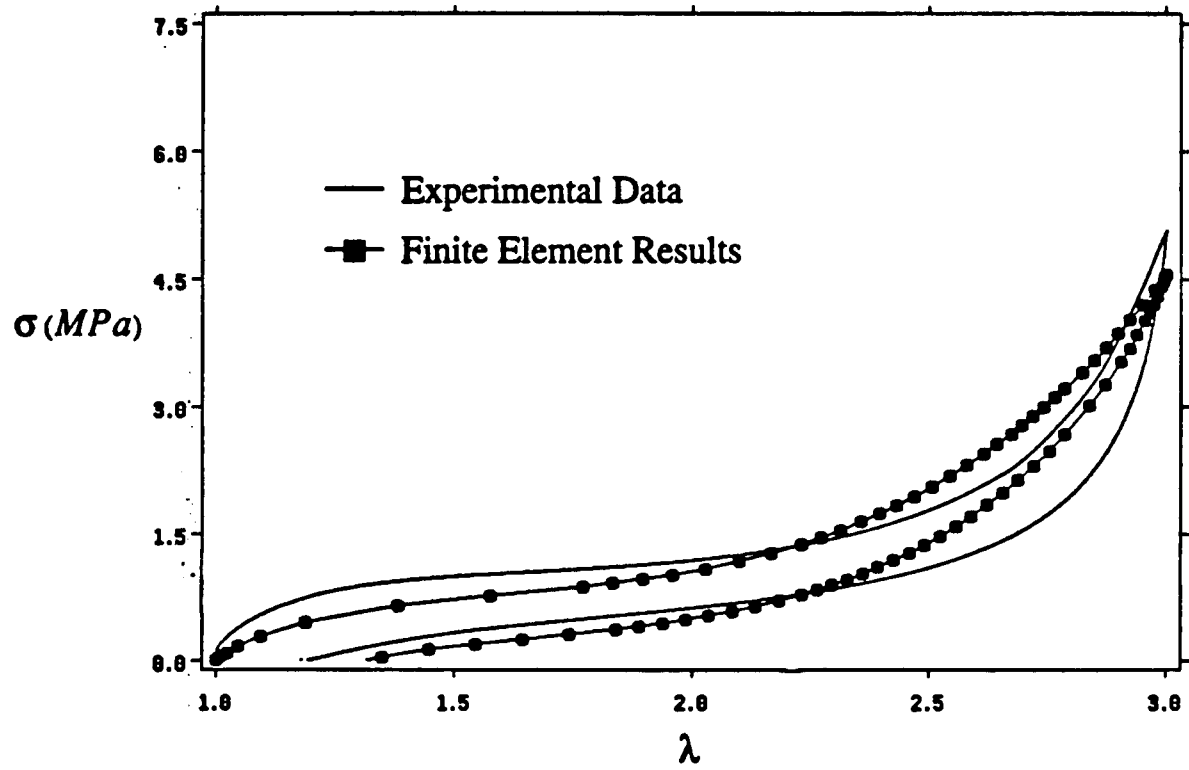Figure 1: The J-integral for a crack advancing in the x_1 direction.

Figure 2: A comparison of predicted and experimental material behavior for a single cycle hysteresis loop.
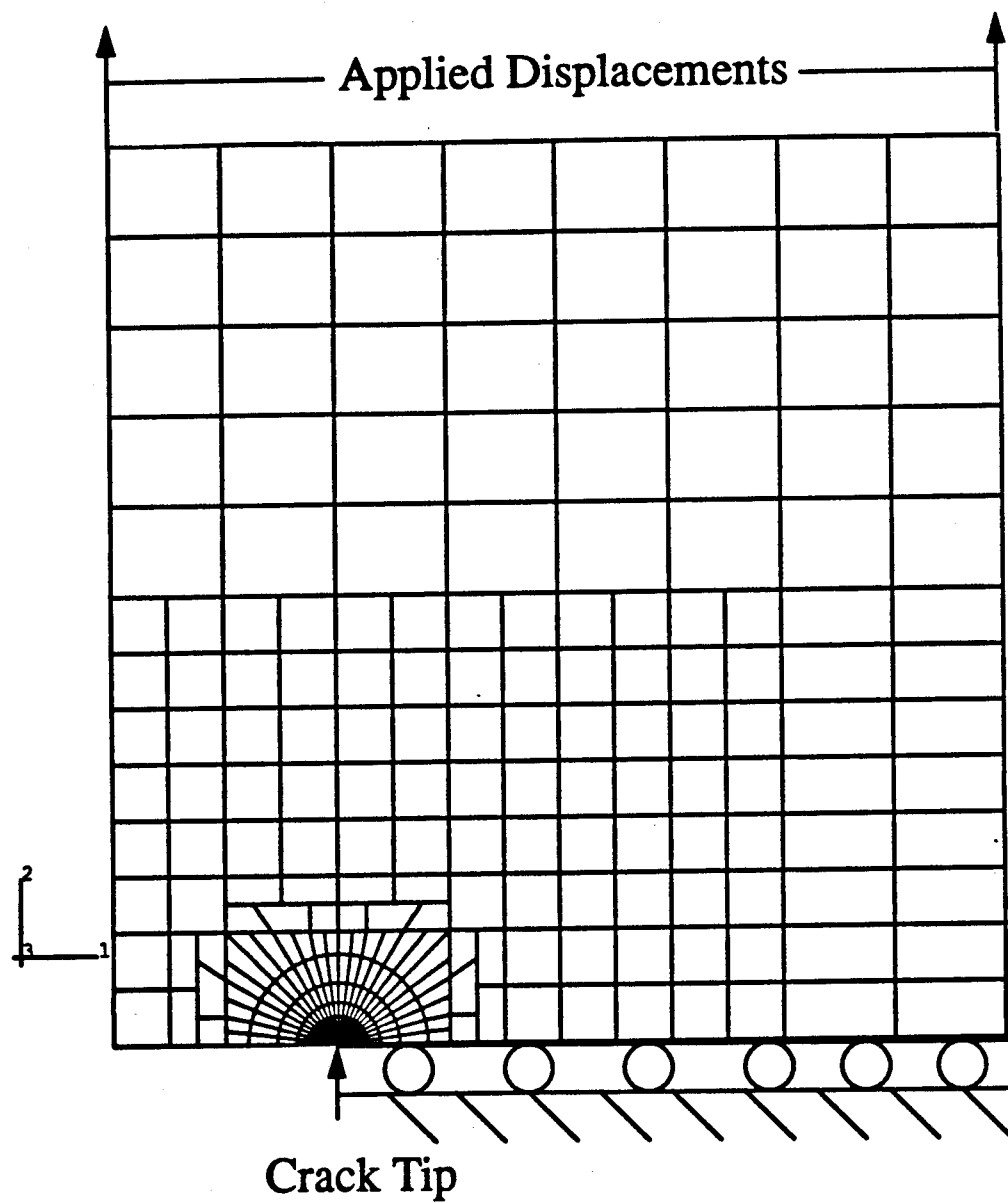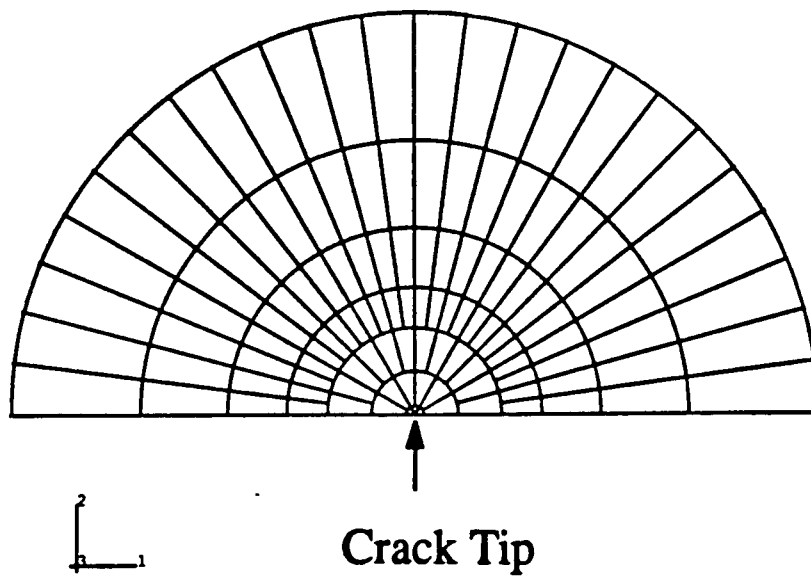
Figure 3: Finite element model.
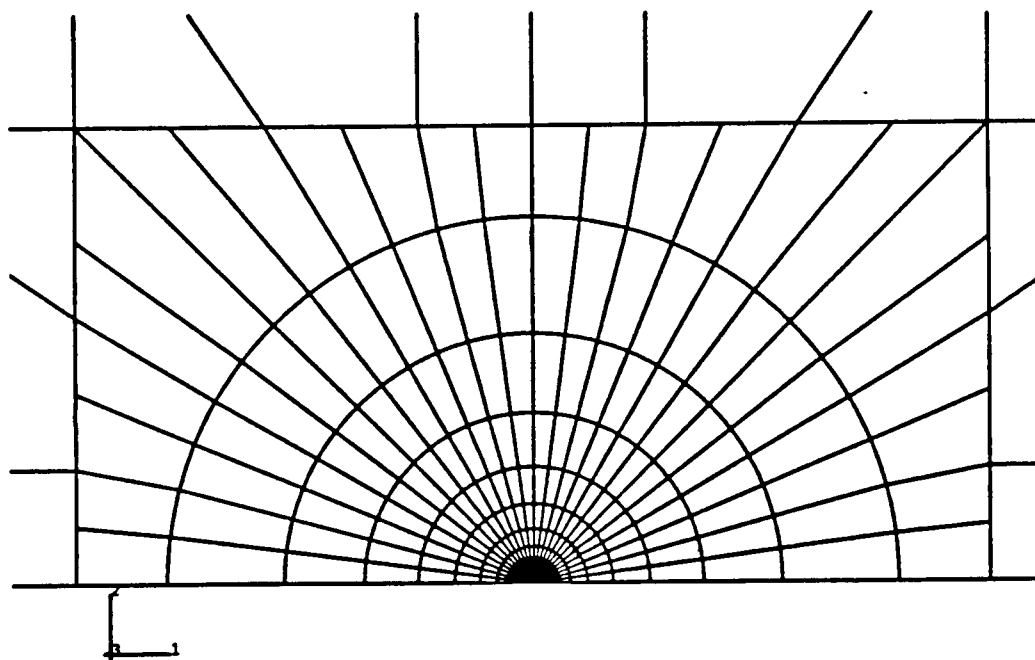
(a)

Crack Tip

(b)

Figure 4: The finite element mesh in the crack tip region: (a) shows the coarse mesh surrounding the crack tip; (b) shows the refined mesh region enclosing the coarse mesh.
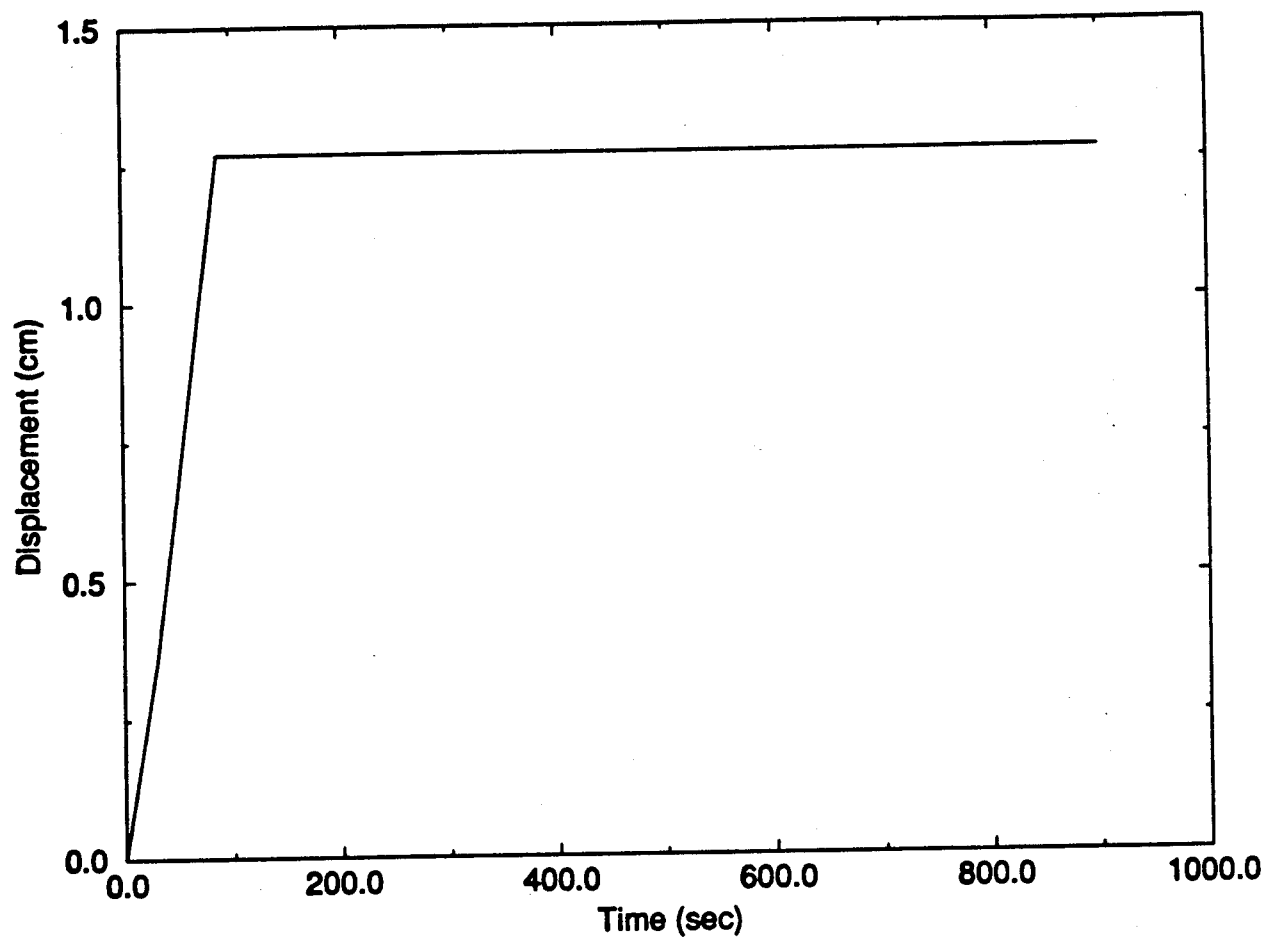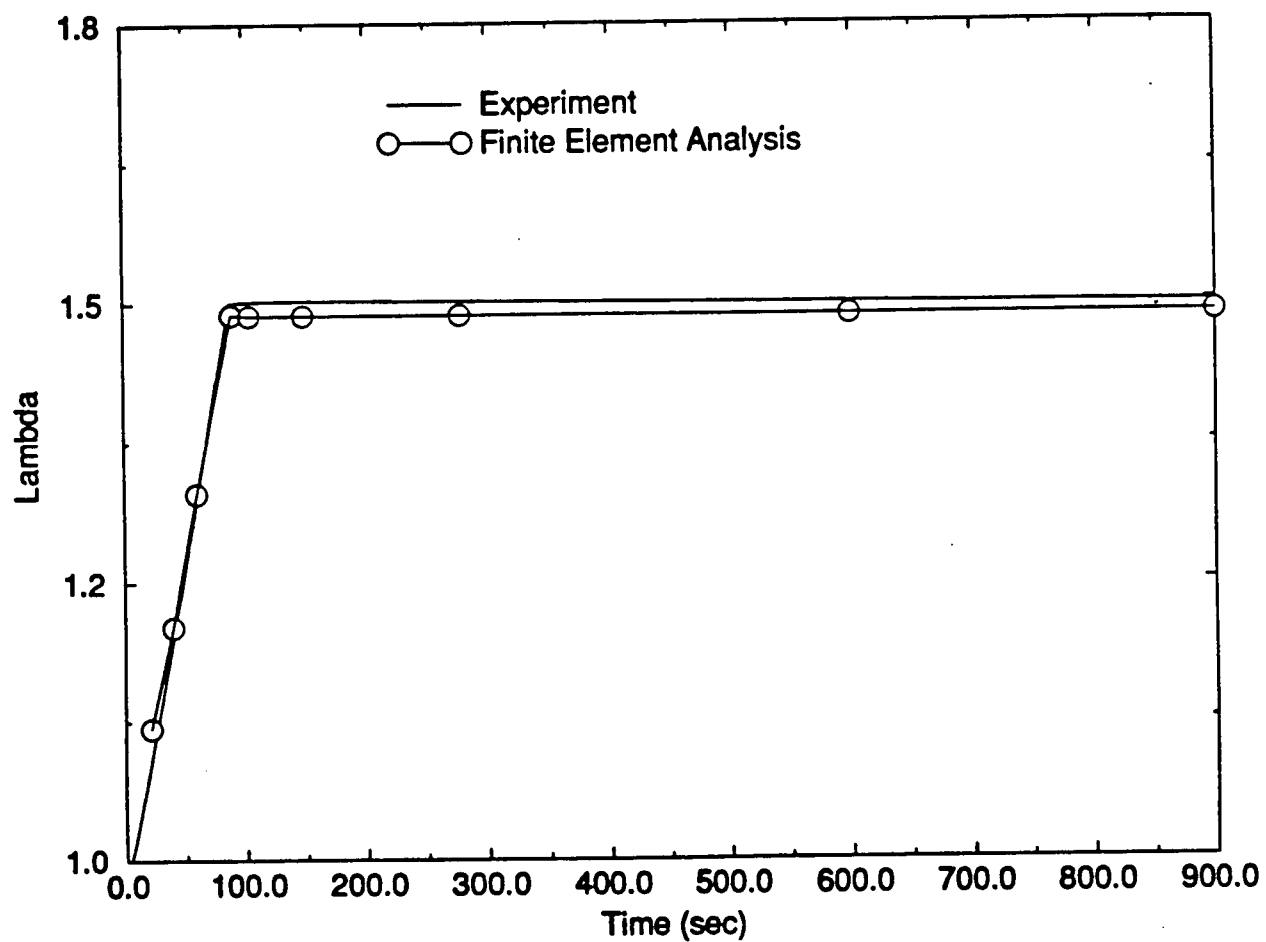
Figure 5: Displacement history.

Figure 6: A comparison of the applied stretch ratios as a function of time.
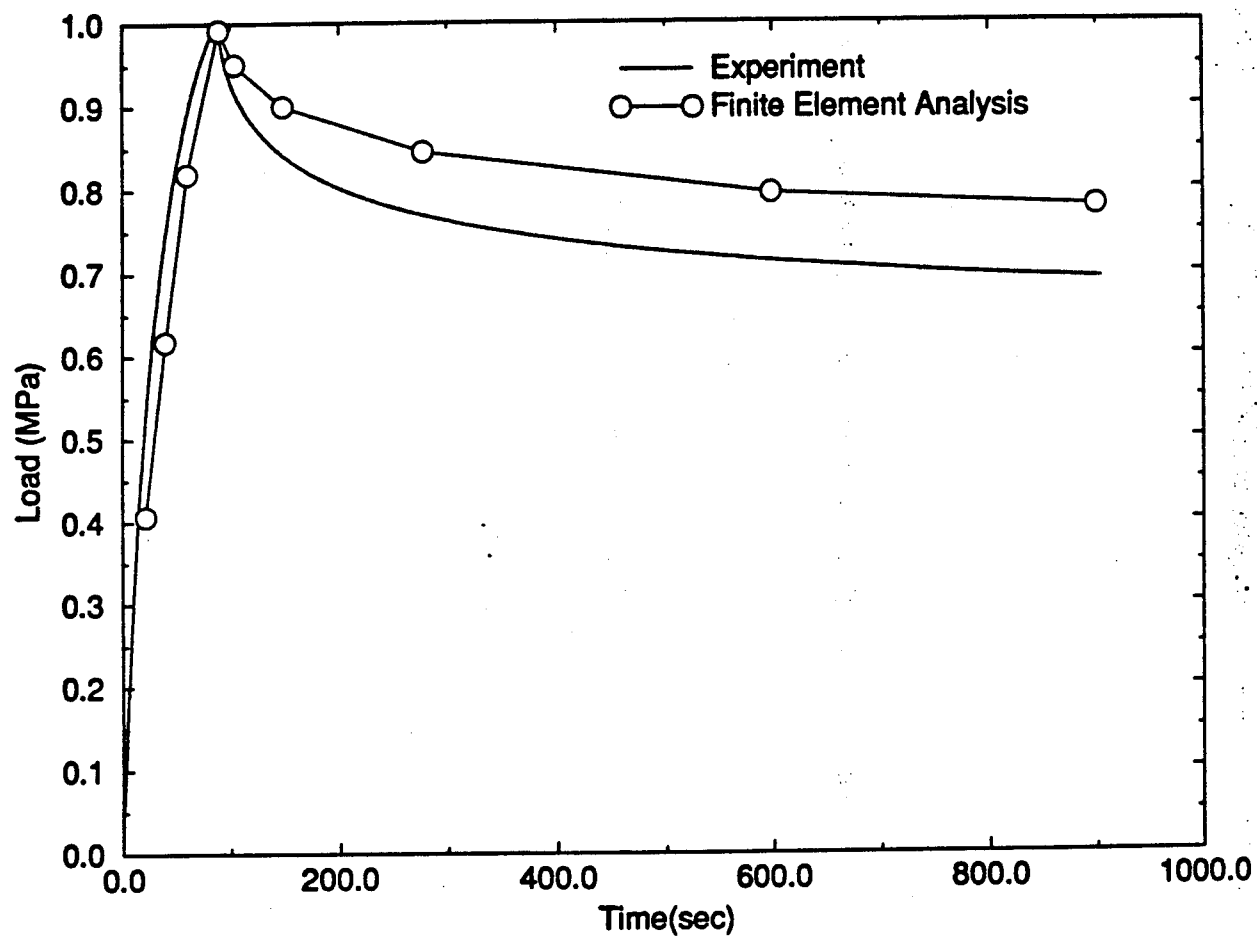
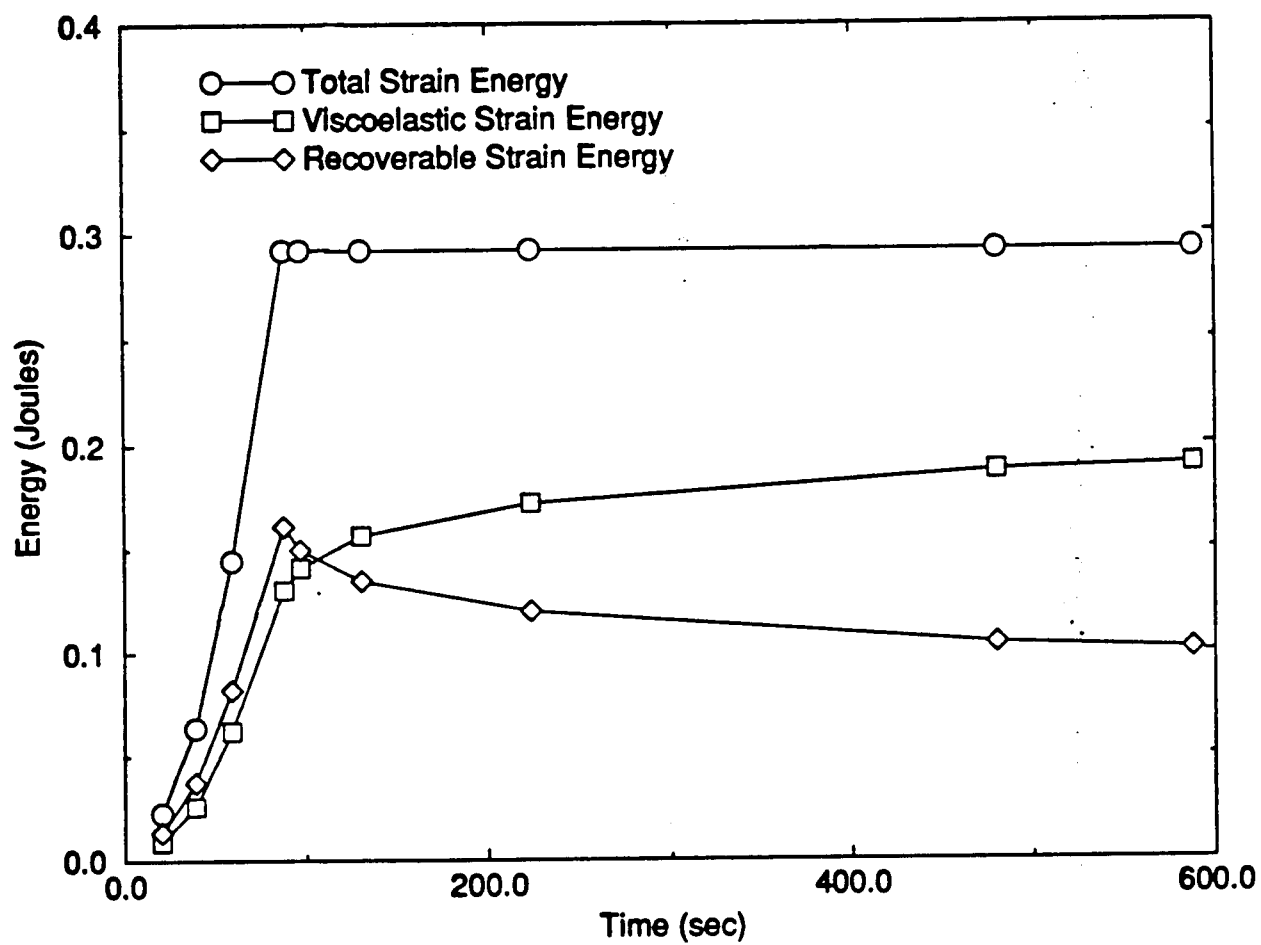Figure 7: A comparison of the applied load as a function of time.

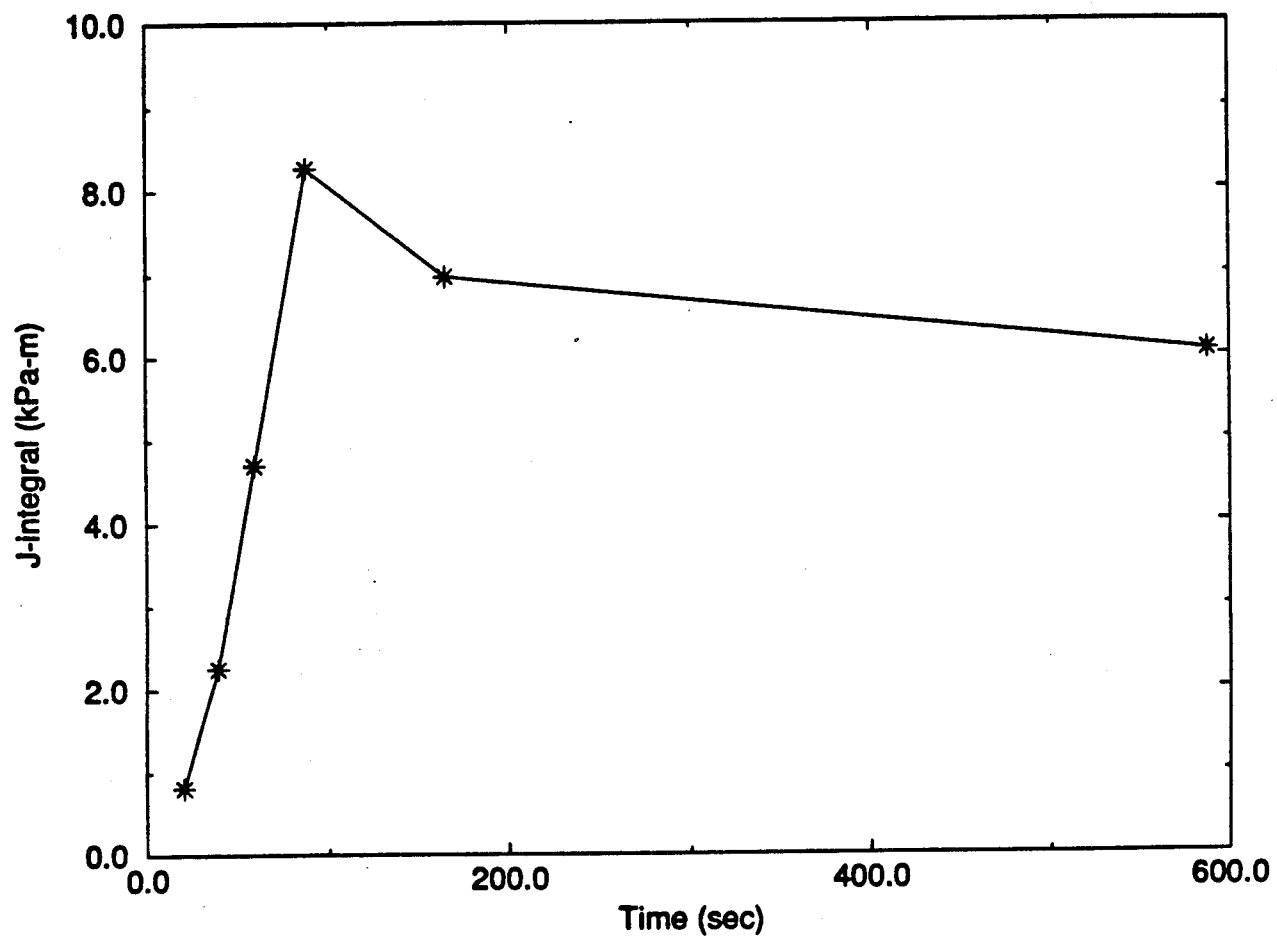Figure 8: A history of energy changes in the finite element analysis.

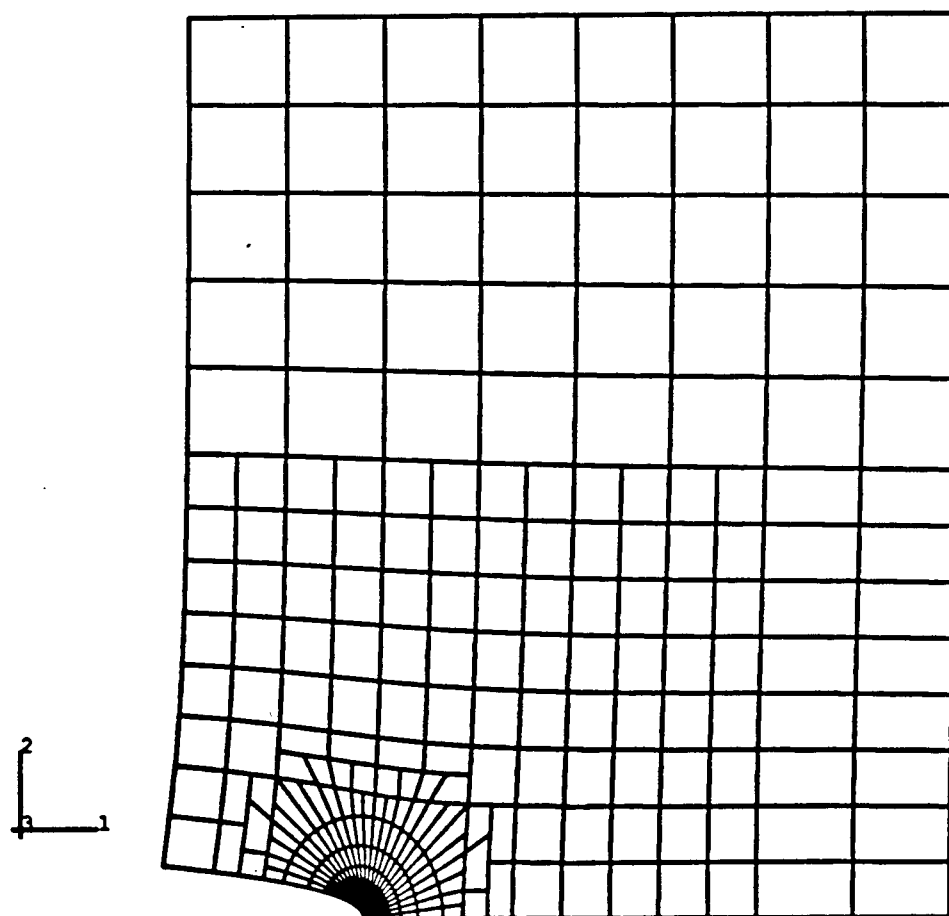Figure 9: The *J*-integral as a function of time.
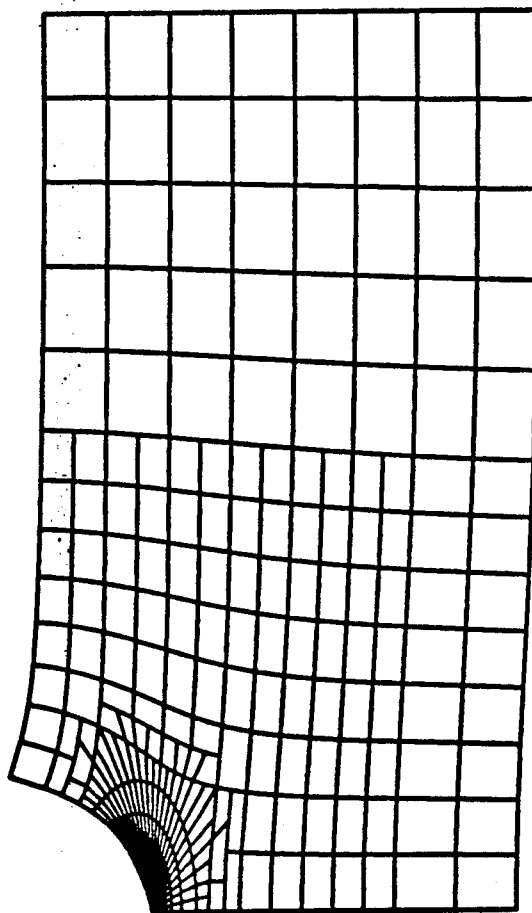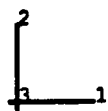
27

Figure 10: The deformed mesh at $t = 21$ sec.

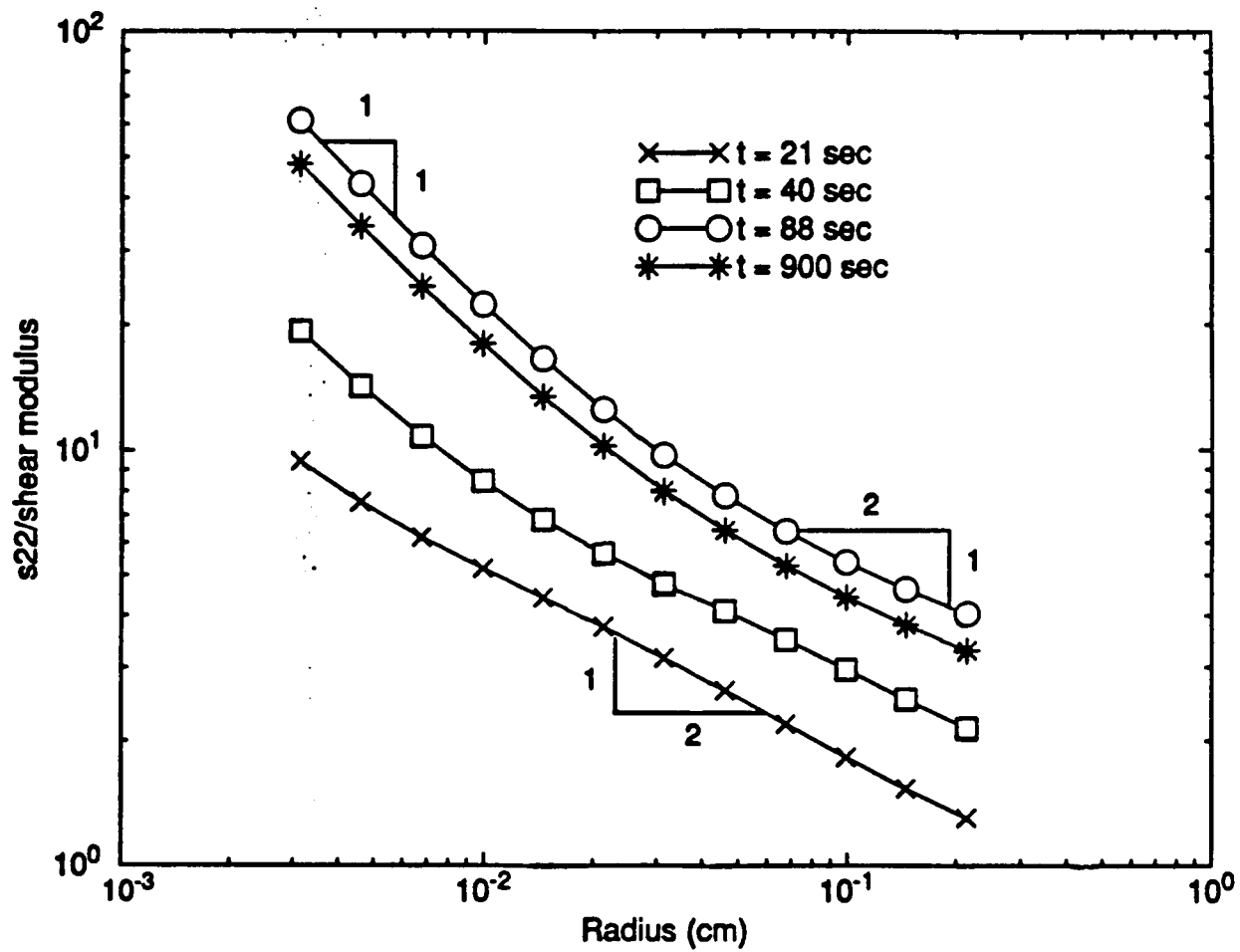Figure 11: The deformed mesh at $t = 88$ sec.

Figure 12: The stress component S_{22} as a function of radial distance from the crack tip at $\theta = 71$ degrees.
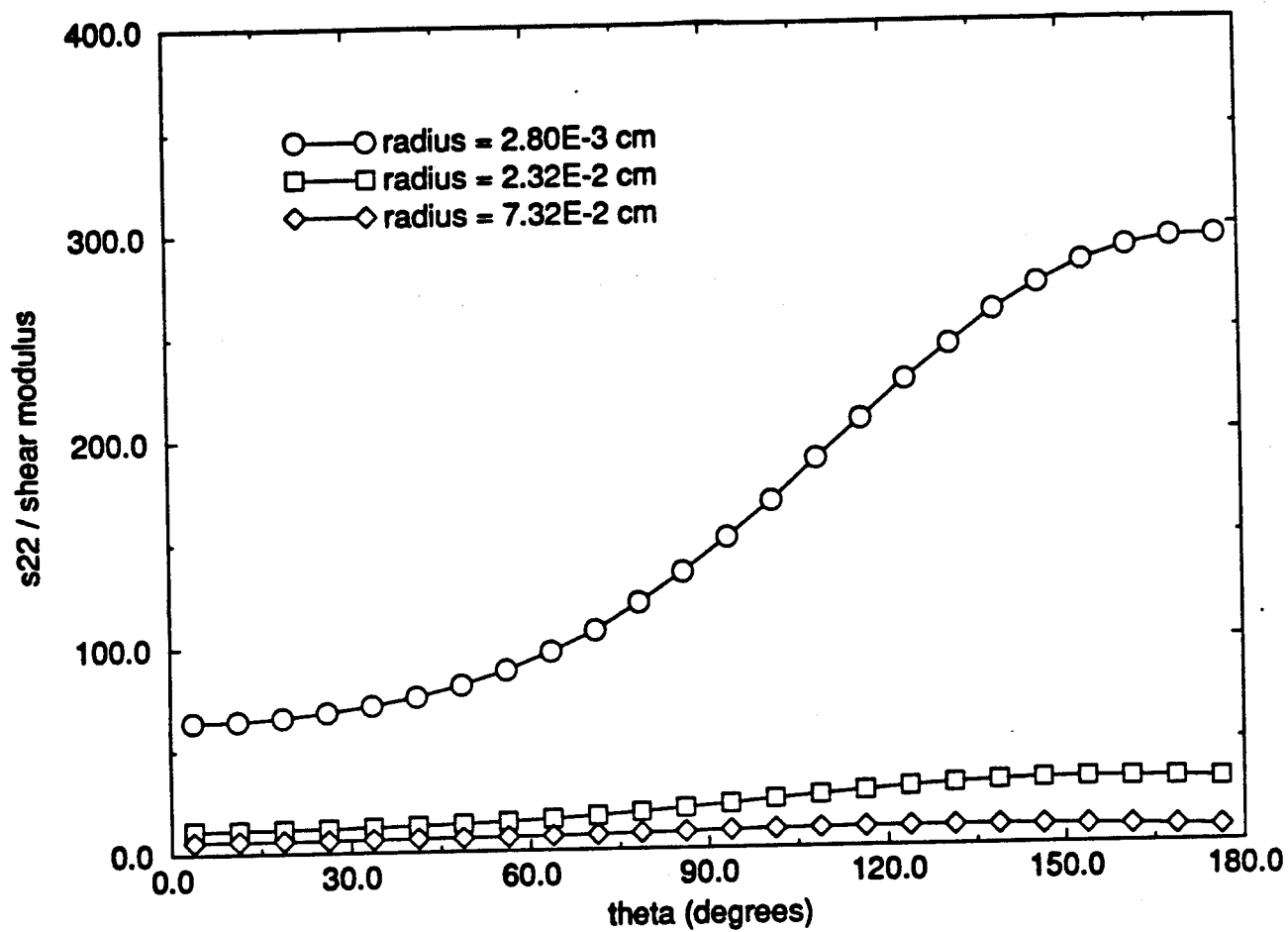
Figure 13: Circumferential plots of S_{22} as a function of polar angle at $t = 88$ sec.
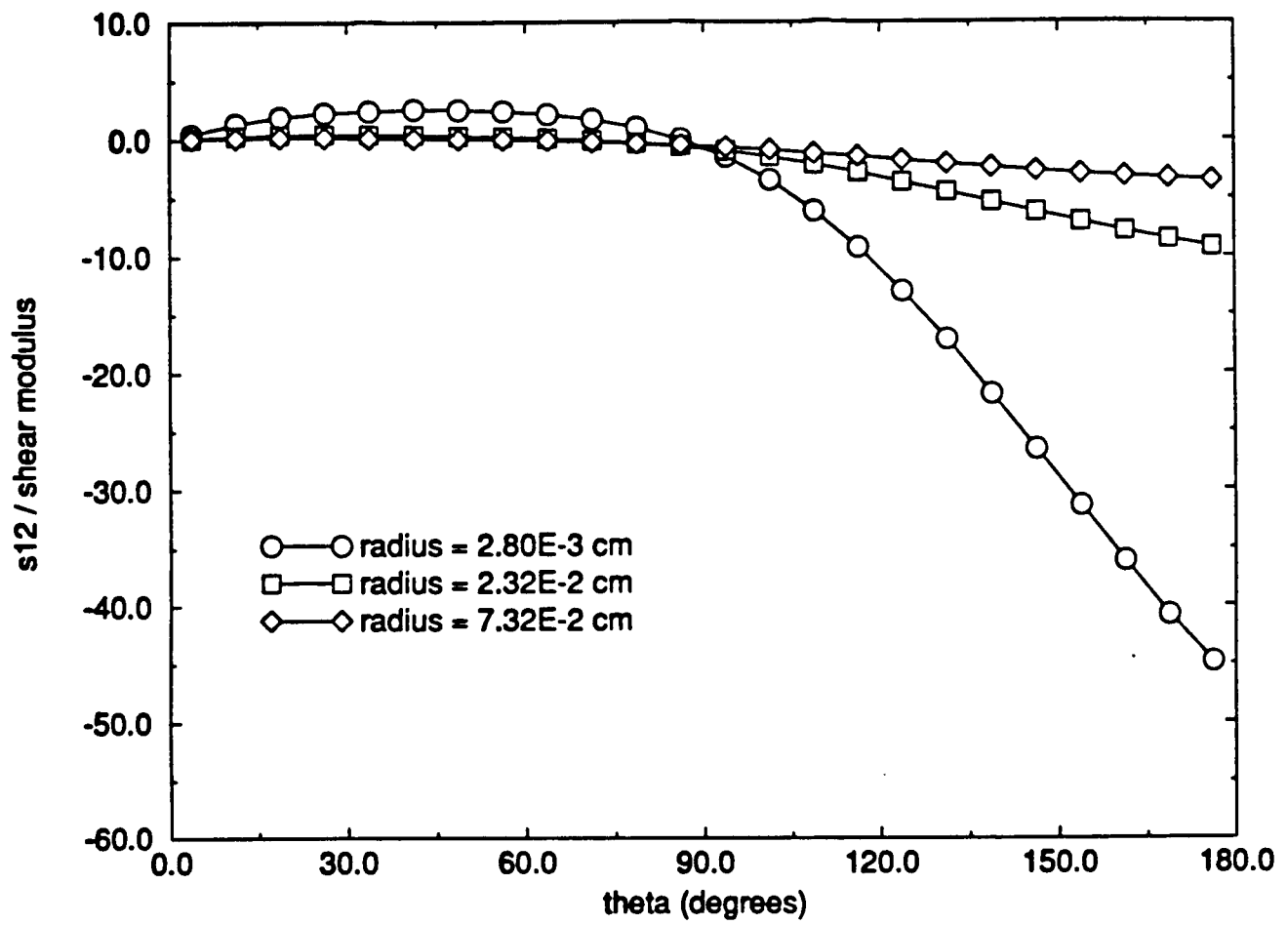
Figure 14: Circumferential plots of S_{12} as a function of polar angle at $t = 88$ sec.
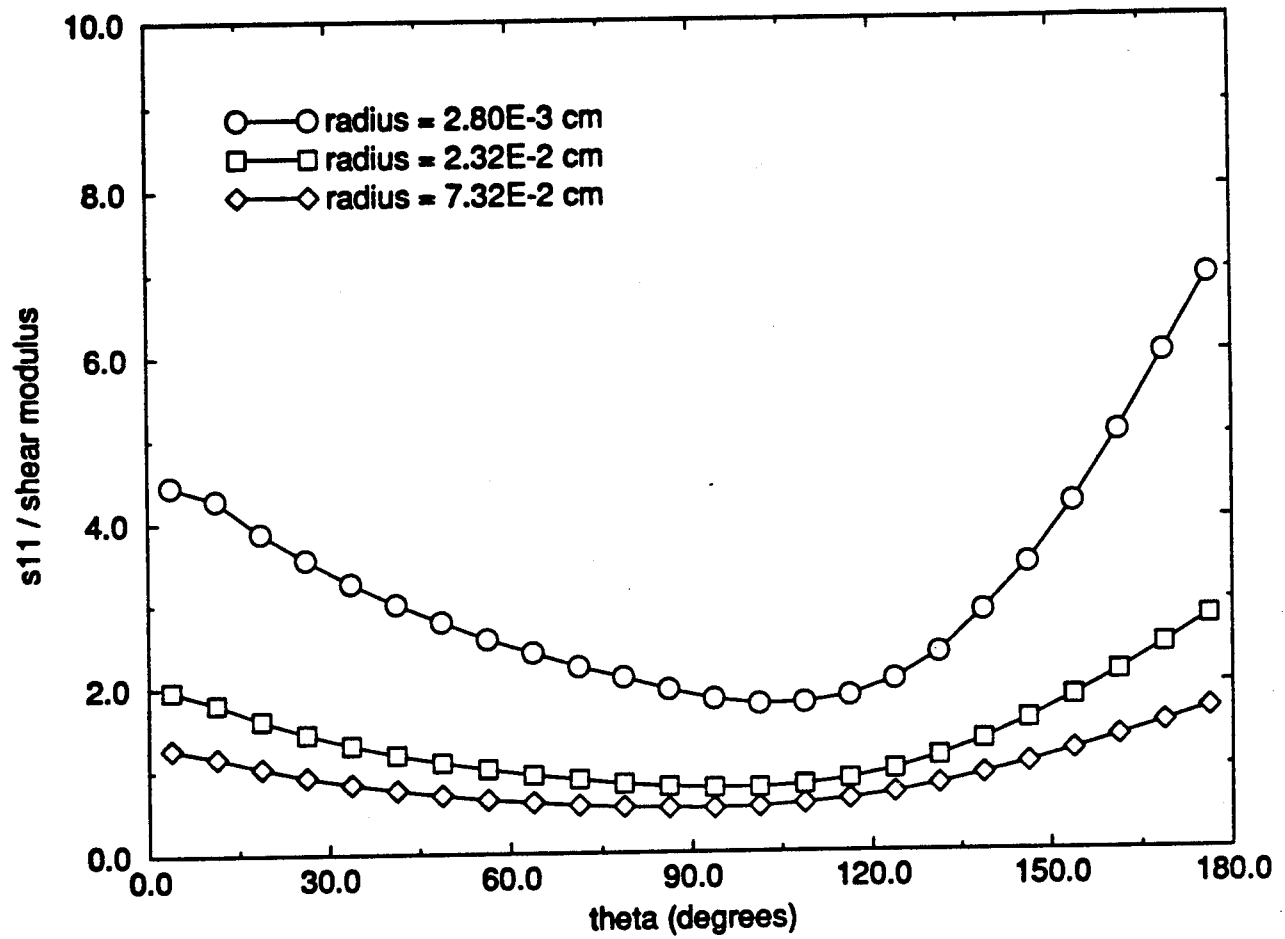
Figure 15: Circumferential plots of S_{11} as a function of polar angle at $t = 88$ sec.

DISTRIBUTION LIST

No. of Copies	To
1	Office of the Under Secretary of Defense for Research and Engineering, The Pentagon, Washington, DC 20301

Director, U.S. Army Research Laboratory, 2800 Powder Mill Road, Adelphi, MD 20783-1197
1 ATTN: AMSRL-OP-SD-TP, Technical Publishing Branch
1　　　　AMSRL-OP-SD-TA, Records Management
1　　　　AMSRL-OP-SD-TL, Technical Library

Commander, Defense Technical Information Center, Cameron Station, Building 5,
5010 Duke Street, Alexandria, VA 23304-6145
2 ATTN: DTIC-FDAC

1 MIA/CINDAS, Purdue University, 2595 Yeager Road, West Lafayette, IN 47905

Commander, Army Research Office, P.O. Box 12211, Research Triangle Park,
NC 27709-2211
1 ATTN: Information Processing Office

Commander, U.S. Army Materiel Command, 5001 Eisenhower Avenue, Alexandria, VA 22333
1 ATTN: AMCSCI

Commander, U.S. Army Materiel Systems Analysis Activity, Aberdeen Proving Ground,
MD 21005
1 ATTN: AMXSY-MP, H. Cohen

Commander, U.S. Army Missile Command, Redstone Arsenal, AL 35809
1 ATTN: AMSMI-RD-CS-R/Doc

Commander, U.S. Army Armament, Munitions and Chemical Command, Dover, NJ 07801
1 ATTN: Technical Library

Commander, U.S. Army Natick Research, Development and Engineering Center
Natick, MA 01760-5010
1 ATTN: SATNC-MI, Technical Library

Commander, U.S. Army Satellite Communications Agency, Fort Monmouth, NJ 07703
1 ATTN: Technical Document Center

Commander, U.S. Army Tank-Automotive Command, Warren, MI 48397-5000
1 ATTN: AMSTA-ZSK
1　　　　AMSTA-TSL, Technical Library

President, Airborne, Electronics and Special Warfare Board, Fort Bragg, NC 28307
1 ATTN: Library

Director, U.S. Army Research Laboratory, Weapons Technology, Aberdeen Proving Ground,
MD 21005-5066
1 ATTN: AMSRL-WT

No. of Copies	To

Commander, Dugway Proving Ground, UT 84022
1   ATTN: Technical Library, Technical Information Division

Commander, U.S. Army Research Laboratory, 2800 Powder Mill Road, Adelphi, MD 20783
1   ATTN: AMSRL-SS

Director, Benet Weapons Laboratory, LCWSL, USA AMCCOM, Watervliet, NY 12189
1   ATTN: AMSMC-LCB-TL
1   AMSMC-LCB-R
1   AMSMC-LCB-RM
1   AMSMC-LCB-RP

Commander, U.S. Army Foreign Science and Technology Center, 220 7th Street, N.E., Charlottesville, VA 22901-5396
3   ATTN: AIFRTC, Applied Technologies Branch, Gerald Schlesinger

Commander, U.S. Army Aeromedical Research Unit, P.O. Box 577, Fort Rucker, AL 36360
1   ATTN: Technical Library

U.S. Army Aviation Training Library, Fort Rucker, AL 36360
1   ATTN: Building 5906-5907

Commander, U.S. Army Agency for Aviation Safety, Fort Rucker, AL 3636
1   ATTN: Technical Library

Commander, Clarke Engineer School Library, 3202 Nebraska Ave., N., Fort Leonard Wood, MO 65473-5000
1   ATTN: Library

Commander, U.S. Army Engineer Waterways Experiment Station, P.O. Box 631, Vicksburg, MS 39180
1   ATTN: Research Center Library

Commandant, U.S. Army Quartermaster School, Fort Lee, VA 23801
1   ATTN: Quartermaster School Library

Naval Research Laboratory, Washington, DC 20375
1   ATTN: Code 6384

Chief of Naval Research, Arlington, VA 22217
1   ATTN: Code 471

Commander, U.S. Air Force Wright Research and Development Center, Wright-Patterson Air Force Base, OH 45433-6523
1   ATTN: WRDC/MLLP, M. Forney, Jr.
1   WRDC/MLBC, Mr. Stanley Schulman

U.S. Department of Commerce, National Institute of Standards and Technology, Gaithersburg, MD 20899
1   ATTN: Stephen M Hsu, Chief, Ceramics Division, Institute for Materials Science and Engineering

No. of Copies	To
1	Committee on Marine Structures, Marine Board, National Research Council, 2101 Constitution Avenue, N.W., Washington, DC 20418
1	Materials Sciences Corporation, Suite 250, 500 Office Center Drive, Fort Washington, PA 19034
1	Charles Stark Draper Laboratory, 555 Technology Square, Cambridge, MA 02139
1	General Dynamics, Convair Aerospace Division, P.O. Box 748, Fort Worth, TX 76101 ATTN: Mfg. Engineering Technical Library
1	Plastics Technical Evaluation Center, PLASTEC, ARDEC, Bldg. 355N, Picatinny Arsenal, NJ 07806-5000 ATTN: Harry Pebly
1	Department of the Army, Aerostructures Directorate, MS-266, U.S. Army Aviation R&T Activity - AVSCOM, Langley Research Center, Hampton, VA 23665-5225
1	NASA - Langley Research Center, Hampton, VA 23665-5255
1	U.S. Army Vehicle Propulsion Directorate, NASA Lewis Research Center, 2100 Brookpark Road, Cleveland, OH 44135-3191 ATTN: AMSRL-VP
1	Director, Defense Intelligence Agency, Washington, DC 20340-6053 ATTN: ODT-5A, Mr. Frank Jaeger
1	U.S. Army Communications and Electronics Command, Fort Monmouth, NJ 07703 ATTN: Technical Library
1	U.S. Army Research Laboratory, Electronic Power Sources Directorate, Fort Monmouth, NJ 07703 ATTN: Technical Library
2	Director, U.S. Army Research Laboratory, Watertown, MA 02172-0001 ATTN: AMSRL-OP-WT-IS, Technical Library
10	Authors